Material Point Modeling of Sand Column Collapse

Corné J. Coetzee * and Matthew D. Purvance

Posted Date: 7 May 2026

doi: 10.20944/preprints202605.0398.v1

Keywords: material point method; sand; column collapse; runout

 doi:10.20944/preprints202605.0398.v1

Article

Material Point Modeling of Sand Column Collapse

Corné J. Coetzee [1,*] and Matthew D. Purvance [2]

[1] Department of Mechanical and Mechatronic Engineering, Stellenbosch University, South Africa
[2] Simtra Dynamics LLC, Soda Springs, California, USA
* Correspondence: ccoetzee@sun.ac.za

Abstract

Events such as landslides and slope failures happen suddenly and can be catastrophic. To predict the onset of such events, as well as the flow and final deposition of the material, engineers make use of numerical modeling techniques. These events are associated with large deformation and mesh-based methods, such as the finite element method, are not capable of modeling them due to mesh distortion. The material point method (MPM) is a particle-based continuum method capable of modeling large deformation and material flow. In this paper, MPM is used to model the sudden and dynamic flow of material by modeling the collapse and runout of a non-cohesive sand column. The results from two- and three-dimensional models are compared to experiments, showing that MPM accurately predicts the free-surface profile of the material during collapse. Furthermore, the model accurately predicts the runout distance with an error of less than 5 %.

Keywords: material point method; sand; column collapse; runout

1. Introduction

A landslide is the sudden movement of rock, soil, and/or debris down a slope, often triggered by heavy rainfall, earthquakes, or human activity. Similar events include slope failures, avalanches, and debris flows. These events are dangerous because they can happen quickly and without much warning, destroying homes, roads, and infrastructure in the flow path. To support risk assessment, develop mitigation measures and strategies, engineers turn to numerical modeling to forecast the occurrence and extent of damage associated with such events.

Mesh-based continuum methods, such as the finite element method (FEM), are often used to predict the onset of slope failure. Such methods have limited ability to predict post-failure material flow, though, due to mesh distortion. Meshless or particle-based continuum methods, on the other hand, can model large deformation and the very large-strain material flow, predicting the end result of an event such as a slope failure or landslide. The material point method (MPM), first introduced by Sulsky et al. [1–3], is such a particle-based method, using material points as a spatial discretization of the material in conjunction with a fixed background grid composed of nodes. This strategy allows for Lagrangian-type tracking of material deformation while the Eulerian background grid is convenient for calculating gradients and solving the equation of motion. Unlike some other particle-based methods (e.g., smooth particle hydrodynamics), no neighbor searching is needed. MPM does require the projection of mass, momentum, and force from material points to grid nodes, where the momentum equation is solved; the updated velocity is subsequently projected back to the material points and, as a result, the background grid does not deform. All state variables including mass, velocity, momentum, strain, and stress are defined at the material points. MPM is commonly used to model various geotechnical applications, including slope failure [4–13].

It is of vital importance to validate all numerical models, the gold standard being to compare numerical results with experimental outcomes. Granular column collapse is a well established experiment where a column of granular material is suddenly released on a flat surface, resulting in a collapse of the column and the runout of material. This sudden and highly dynamic event is representative of a

 doi:10.20944/preprints202605.0398.v1

slope failure or landslide, and suitable to validate the accuracy with which numerical methods can predict the flow of material.

Various studies have used MPM to model granular column collapse, for example [14–21]. However, all of these studies use two-dimensional models, and not all of them validate their results against experiments. Lube et al. [22,23] performed a series of well-documented experiments under two-dimensional conditions, using a range of column aspect ratios (initial height to width). Sołowski and Sloan [24,25] and Hamad et al. [26], modeled one of these experiments to validate their two-dimensional MPM models. Lube et al. [27] performed a similar series of laboratory experiments for three-dimensional axis-symmetric columns which have yet to be modeled. According to the authors' knowledge, this is the first study to simulate column collapse using both two- and three-dimensional MPM models over a large range of column aspect ratios, comparing the numerical results with experimental measurements.

2. Materials and Methods

2.1. The Material Point Method

The are a number of MPM implementation options and combinations, such as the updated Lagrangian or total Lagrangian approaches, the update-stress first (USF) or update-stress-last (USL) schemes, the use of a fluid-implicit-particle (FLIP) or particle-in-cell (PIC) velocity update, and various choices of interpolation (basis) functions, among others. In this work the updated Lagrangian formulation is used with explicit time integration and the USL scheme. Quadratic B-spline basis functions are used with Taylor particle-in-cell velocity projection (TPIC). To avoid any confusion, the specific implementation used in this work is presented below.

2.1.1. Conservation Equations

The strong form of the governing equations include the conservation of mass,

$$\frac{\partial \rho}{\partial t} + \rho \nabla \cdot \mathbf{v} = \mathbf{0} \tag{1}$$

and the conservation of momentum,

$$\rho \frac{\partial \mathbf{v}}{\partial t} = \nabla \cdot \boldsymbol{\sigma} + \rho \mathbf{b} \tag{2}$$

where $\rho(\mathbf{x}, t)$ is the density field at the material position $\mathbf{x}$ and time t, ∇ is the divergence operator, $\mathbf{v}(\mathbf{x}, t)$ is the velocity field, $\boldsymbol{\sigma}(\mathbf{x}, t)$ is the stress field, and $\mathbf{b}(\mathbf{x}, t)$ is the body force vector due to gravitational acceleration. Furthermore, the rate of deformation tensor $\mathbf{D}(\mathbf{x}, t)$ (strain rate tensor $\dot{\boldsymbol{\varepsilon}}$) is related to the velocity,

$$\dot{\boldsymbol{\varepsilon}} := \mathbf{D} = \frac{1}{2}\left[(\nabla \mathbf{v}) + (\nabla \mathbf{v})^{\mathrm{T}}\right] \tag{3}$$

Using a Lagrangian approach with the material points having constant mass automatically satisfies conservation of mass. Assuming an isothermal system, the energy equation is also not solved. The weak form of the momentum equation is obtained by multiplying Equation 2 by a test function $\mathbf{t}(\mathbf{x})$ (virtual displacement field), integrating over the volume of the current configuration $\boldsymbol{\Omega}$, and using integration by parts,

$$\int_{\Omega} \rho \mathbf{t} \cdot \mathbf{a} \, \mathrm{d}\Omega = -\int_{\Omega} \rho \boldsymbol{\sigma}^{s} : \nabla \mathbf{t} \, \mathrm{d}\Omega + \int_{\Gamma} \mathbf{t} \cdot \boldsymbol{\tau} \, \mathrm{d}\Gamma + \int_{\Omega} \rho \mathbf{t} \cdot \mathbf{b} \, \mathrm{d}\Omega \tag{4}$$

where $\mathbf{a}(\mathbf{x}, t) = \frac{\partial \mathbf{v}}{\partial t}$ is the acceleration field, $\boldsymbol{\sigma}^{s} = \frac{\boldsymbol{\sigma}}{\rho}$ is the specific Cauchy stress tensor, and $\boldsymbol{\tau}$ is the traction vector acting on the boundary $\boldsymbol{\Gamma}$.

 doi:10.20944/preprints202605.0398.v1

2.1.2. Spatial Discretization

The material domain $\mathbf{\Omega}$ is discretized by a set of material points. Each material point has a sub-domain $\mathbf{\Omega}_p$ as shown in Figure 1. The whole mass of the sub-domain m_p is concentrated at the material point position, and the density field can be written as,

$$\rho(\mathbf{x}, t) = \sum_{p=1}^{n_p} m_p \delta(\mathbf{x} - \mathbf{x}_p) \tag{5}$$

where n_p is the total number of material points and $\delta(\mathbf{x})$ is the Dirac delta function [28]. Substituting Equation 5 into Equation 4, and ignoring traction for the moment, transforms the continuous integrals to discrete summation over the material points,

$$\sum_{p=1}^{n_p} m_p \mathbf{t}(\mathbf{x}_p) \cdot \mathbf{a}(\mathbf{x}_p) = -\sum_{p=1}^{n_p} m_p \boldsymbol{\sigma}^s(\mathbf{x}_p) : \nabla \mathbf{t}(\mathbf{x})\Big|_{\mathbf{x}=\mathbf{x}_p} + \sum_{p=1}^{n_p} m_p \mathbf{t}(\mathbf{x}_p) \cdot \mathbf{b}(\mathbf{x}_p) \tag{6}$$

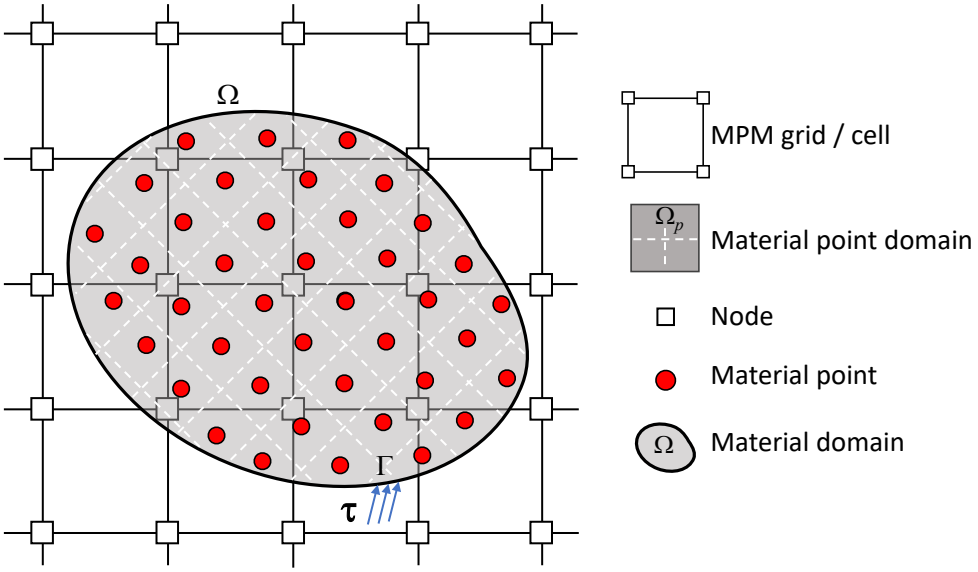

Figure 1. MPM double-discretization using material points and a computational grid.

To interpolate spatially-varying fields and approximate their spatial gradients, a background grid or mesh is introduced, Figure 1. The mesh with n_n nodes has a basis or interpolation function $N_i(\mathbf{x})$ associated with each node i. When the position corresponds to that of a material point, $\mathbf{x} = \mathbf{x}_p$, the following shorthand notation is used to define the interpolation weight,

$$w_{ip} := N_i(\mathbf{x}_p) \tag{7}$$

and similarly the weight gradients are given by,

$$\nabla w_{ip} := \nabla N_i(\mathbf{x})\Big|_{\mathbf{x}=\mathbf{x}_p} \tag{8}$$

The virtual displacement field at the material point position $\mathbf{t}(\mathbf{x}_p)$, for example, can be interpolated from the nodal virtual displacements $\mathbf{t}_i$,

$$\mathbf{t}(\mathbf{x}_p) = \sum_{i=1}^{n_n} w_{ip} \mathbf{t}_i \tag{9}$$

 doi:10.20944/preprints202605.0398.v1

with the spatial derivative given by the tensor,

$$\nabla \mathbf{t}(\mathbf{x}_p) = \sum_{i=1}^{n_n} \mathbf{t}_i \otimes \nabla w_{ip} \tag{10}$$

where $\otimes$ denotes the outer product. Using Equation 9 and Equation 10 and recognising that any arbitrary virtual displacement can be used, Equation 6 can be written as,

$$\sum_{j=1}^{n_n} m_{ij} \mathbf{a}_j = \mathbf{f}_i^{\text{int}} + \mathbf{f}_i^{\text{ext}} \tag{11}$$

where the consistent mass matrix is given by,

$$m_{ij} = \sum_{p=1}^{n_p} m_p w_{ip} w_{jp} \tag{12}$$

and the internal force vector is given by,

$$\mathbf{f}_i^{\text{int}} = -\sum_{p=1}^{n_p} V_p \boldsymbol{\sigma}_p \cdot \nabla w_{ip} \tag{13}$$

where $V_p = \frac{m_p}{\rho_p}$ is the volume of the material point and $\boldsymbol{\sigma}_p := \boldsymbol{\sigma}(\mathbf{x}_p)$. The external force vector is given by,

$$\mathbf{f}_i^{\text{ext}} = \sum_{p=1}^{n_p} w_{ip} m_p \mathbf{b}_p \tag{14}$$

where $\mathbf{b}_p := \mathbf{b}(\mathbf{x}_p)$ is the body force due to gravity. In MPM, it is customary to replace the consistent mass matrix m_{ij} with the diagonal *lumped* mass matrix m_i,

$$m_i = \sum_{j=1}^{n_n} m_{ij} = \sum_{p=1}^{n_p} m_p w_{ip} \tag{15}$$

The momentum equation (Equation 11) then becomes a system of uncoupled equations,

$$m_i \mathbf{a}_i = \mathbf{f}_i^{\text{ext}} + \mathbf{f}_i^{\text{int}} \tag{16}$$

2.1.3. Grid and Basis Function

A Cartesian background grid with equal node spacing h in all three cardinal directions is used, Figure 1. The original implementations of MPM used a linear basis function ([2,3,29] among many others). However linear basis functions are known to produce the so called *grid-crossing instability* as described by [30] and [31], for example. For this reason the quadratic B-spline basis functions are used in this work, with the one-dimensional function given by [32–34],

$$N_i^{\text{1D}}(r) = \begin{cases} \frac{3}{4} - |r|^2 & 0 \le |r| < \frac{1}{2} \\ \frac{1}{2}\left(\frac{3}{2} - |r|\right)^2 & \frac{1}{2} \le |r| < \frac{3}{2} \\ 0 & \frac{3}{2} \le |r| \end{cases} \tag{17}$$

where $r = \frac{1}{h}(x - x_i)$, h is the node spacing, and x_i the nodal position. The stencil of the 1D basis function has compact support over $x \in [x_i - 3/2h, x_i + 3/2h]$ and spans a total of $3h$. The gradient of the basis function is given by,

 doi:10.20944/preprints202605.0398.v1

$$\nabla N_i^{1\mathrm{D}}(r) = \begin{cases} -2r & 0 \le |r| < \frac{1}{2} \\ (|r| - \frac{3}{2})\mathrm{sign}(r) & \frac{1}{2} \le |r| < \frac{3}{2} \\ 0 & \frac{3}{2} \le |r| \end{cases} \tag{18}$$

Two- and three-dimensional basis functions are computed by taking the product of the one-dimensional basis functions. The support of the B-splines is larger than the node spacing h, so the basis functions are truncated at the boundaries of the domain. This truncation results in the situation where the parity of unity is not sustained for weights near the boundary/. The interpolation (kernel) correction proposed by [35] is used to overcome this issue. This kernel correction is only applied when a material point projects to a boundary node, introducing negligible computational overhead.

2.1.4. Cycling (Time Stepping)

The USL scheme is illustrated in Figure 2, where, for illustrative purposes, linear basis functions are assumed; the principles and steps apply to any basis function, including quadratic B-splines. Generally the following four phases can be identified: (1) the point-to-grid (P2G) projection, (2) the grid update, (3) the grid-to-point (G2P) projection, and (4) increment time (superscript n is used to denote discrete times).

Phase 1: Point-to-Grid Projection

Before the equation of motion (Equation 16) is solved at the grid nodes, the necessary information must first be projected from the material points to the nodes. The grid is initialized by setting the nodal positions $\mathbf{x}_i^0$ and the initial nodal velocity $\mathbf{v}_i^0 = 0$ and mass $m_i^0 = 0$, Figure 2(a). At timestep n each material point has a known position $\mathbf{x}_p^n$ and stores a constant mass m_p and a velocity $\mathbf{v}_p^n$. The weights w_{ip}^n are calculated using the basis function in Equation 17 (and the definition in Equation 7). The mass is then projected to grid node i by summing over all the materials points within the node's stencil (Equation 15),

$$m_i^n = \sum_{p=1}^{n_p} m_p w_{ip}^n \tag{19}$$

The material point momentum is projected to the grid nodes,

$$\mathbf{p}_i^n := m_i^n \mathbf{v}_i^n = \sum_{p=1}^{n_p} m_p w_{ip}^n \left(\mathbf{v}_p^n + \nabla \mathbf{v}_p^n (\mathbf{x}_i - \mathbf{x}_p^n) \right) \tag{20}$$

where $\nabla \mathbf{v}_p^n$ is the velocity gradient evaluated at the material point at the end of the previous timestep. Using the velocity gradient in Equation 20, is called the Taylor transfer or Taylor particle-in-cell (TPIC) approach [35–37]. Finally, the nodal velocity is obtained using,

$$\mathbf{v}_i^n = \frac{\mathbf{p}_i^n}{m_i^n} \tag{21}$$

to provide the nodal velocity at the start of the time step, Figure 2(b). Boundary conditions are applied to the nodes by setting $\mathbf{v}_i^n = 0$.

Phase 2: Grid Evolution

The internal and external nodal forces are calculated using Equation 13 and Equation 14 respectively, which provide a means to compute the nodal acceleration $\mathbf{a}_i^n$,

$$\mathbf{a}_i^n = \frac{1}{m_i^n} \left(\mathbf{f}_i^{\mathrm{ext},n} + \mathbf{f}_i^{\mathrm{int},n} + \mathbf{f}_i^{\mathrm{damp},n} \right) \tag{22}$$

 doi:10.20944/preprints202605.0398.v1

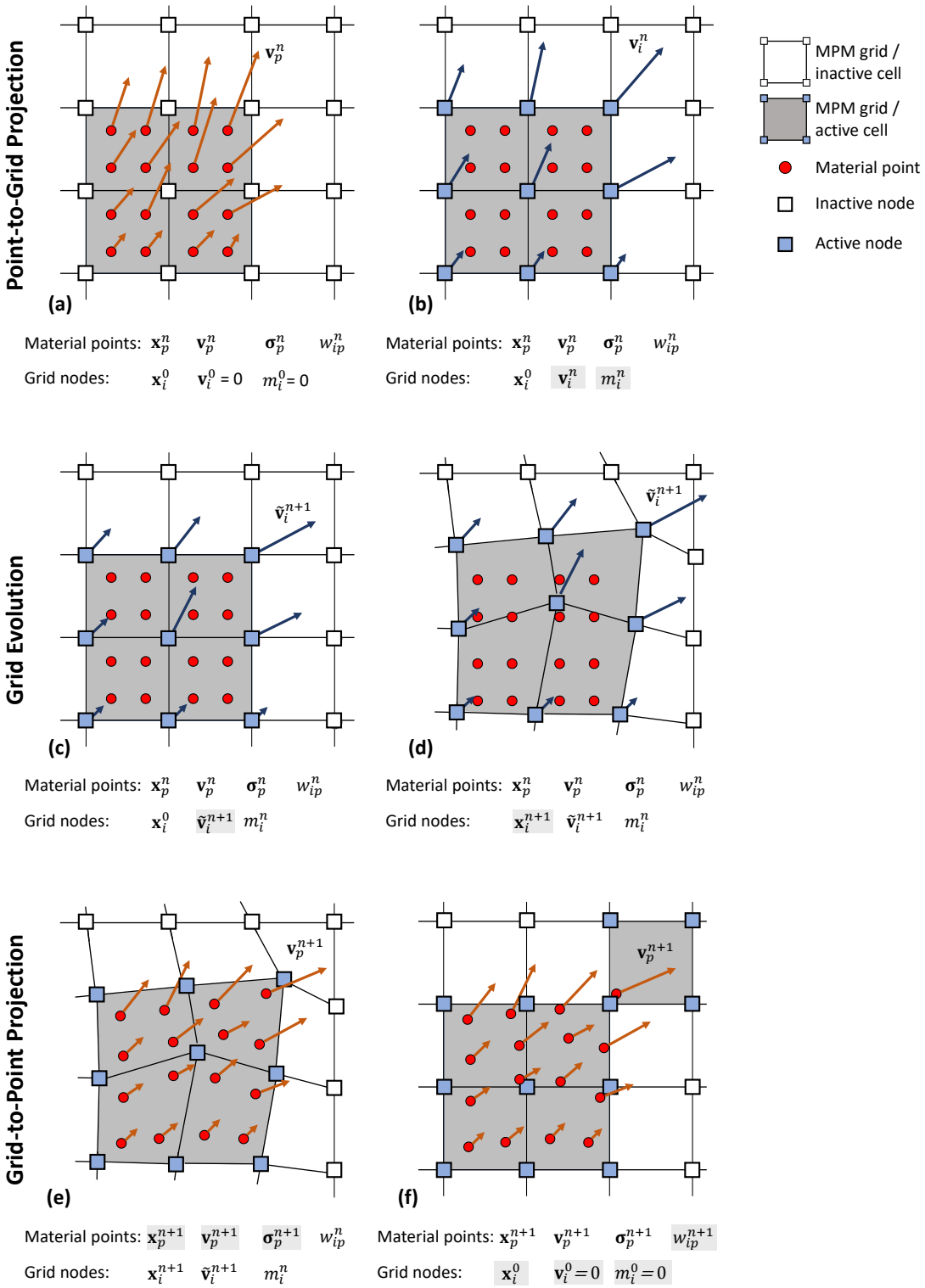

Figure 2. MPM USL time stepping showing the update of selected state variables.

 doi:10.20944/preprints202605.0398.v1

where $\mathbf{f}_i^{\text{damp},n}$ is the local non-viscous damping force given by [38],

$$\mathbf{f}_i^{\text{damp},n} = -\alpha_d \left(\mathbf{f}_i^{\text{ext},n} + \mathbf{f}_i^{\text{int},n} \right) \text{sign}(\mathbf{v}_i^n) \tag{23}$$

where α_d is the damping constant ranging from 0 to 1. Using explicit time integration with timestep Δt, the nodal velocity is then updated, Figure 2(c),

$$\tilde{\mathbf{v}}_i^{n+1} = \mathbf{v}_i^n + \Delta t \mathbf{a}_i^n \tag{24}$$

Boundary conditions are applied to the nodes by setting $\tilde{\mathbf{v}}_i^{n+1} = 0$, and for boundary nodes, the acceleration is recalculated using $\mathbf{a}_i^n = \left(\tilde{\mathbf{v}}_i^{n+1} - \mathbf{v}_i^n \right) / \Delta t$. In theory the nodal position is updated, Figure 2(d),

$$\mathbf{x}_i^{n+1} = \mathbf{x}_i^n + \Delta t \tilde{\mathbf{v}}_i^{n+1} \tag{25}$$

For computational reasons this update is not explicitly performed.

Phase 3: Grid-to-Point Projection

The changes to the grid nodes are projected back to material points where the velocity, position, strain, stress, deformation gradient, volume and density are updated, Figure 2(e). The FLIP update is used where only the change in grid velocity $\left(\tilde{\mathbf{v}}_i^{n+1} - \mathbf{v}_i^n \right)$ is projected to update the material point velocity,

$$\begin{aligned} \mathbf{v}_p^{n+1} &= \mathbf{v}_p^n + \sum_{i=1}^{n_n} w_{ip}^n \left(\tilde{\mathbf{v}}_i^{n+1} - \mathbf{v}_i^n \right) \\ &= \mathbf{v}_p^n + \Delta t \sum_{i=1}^{n_n} w_{ip}^n \mathbf{a}_i^n \end{aligned} \tag{26}$$

A a second-order scheme [39] is used to update the material point position,

$$\mathbf{x}_p^{n+1} = \mathbf{x}_p^n + \Delta t \sum_{i=1}^{n_n} w_{ip}^n \tilde{\mathbf{v}}_i^{n+1} - \Delta t^2 \sum_{i=1}^{n_n} w_{ip}^n \mathbf{a}_i^n \tag{27}$$

The velocity gradient $\nabla \mathbf{v}(\mathbf{x})$ is calculated at material points based on Equation 10,

$$\nabla \mathbf{v}_p^{n+1} = \sum_{i=1}^{n_n} \tilde{\mathbf{v}}_i^{n+1} \otimes \nabla w_{ip}^n \tag{28}$$

The deformation gradient $\mathbf{F}_p^n$ is then updated at the material points,

$$\mathbf{F}_p^{n+1} = \left(\mathbf{I} + \Delta t \, \nabla \mathbf{v}_p^{n+1} \right) \mathbf{F}_p^n \tag{29}$$

where $\mathbf{I}$ is the identity matrix. The volume V_p of the material point is updated using the determinant of the deformation gradient, $J_p := \det(\mathbf{F}_p)$,

$$V_p^{n+1} = J_p^{n+1} V_p^0 \tag{30}$$

and V_p^0 is the point's initial volume. Lastly, the material point's density is updated,

$$\rho_p^{n+1} = \frac{\rho_p^0}{J_p^{n+1}} \tag{31}$$

 doi:10.20944/preprints202605.0398.v1

The rate of deformation (based on Equation 3) at the material point then follows from,

$$\mathbf{D}_p^{n+1} = \frac{1}{2}\left[\nabla \mathbf{v}_p^{n+1} + \left(\nabla \mathbf{v}_p^{n+1}\right)^{\mathrm{T}}\right] \tag{32}$$

The material constitutive model is used to calculate the increment in stress at each material point, where the objective Jaumann stress rate, $\mathring{\boldsymbol{\sigma}}_p^{n+1}\left(\mathbf{D}_p^{n+1}\right)$, is used and the Cauchy stress at the material point is updated,

$$\boldsymbol{\sigma}_p^{n+1} = \boldsymbol{\sigma}_p^n + \Delta t\left(\mathring{\boldsymbol{\sigma}}_p^{n+1} + \mathbf{W}_p^{n+1}\cdot\boldsymbol{\sigma}_p^n - \boldsymbol{\sigma}_p^n\cdot\mathbf{W}_p^{n+1}\right) \tag{33}$$

where $\mathbf{W}_p^{n+1}$ is the spin tensor computed at the material point,

$$\mathbf{W}_p^{n+1} = \frac{1}{2}\left[\nabla \mathbf{v}_p^{n+1} - \left(\nabla \mathbf{v}_p^{n+1}\right)^{\mathrm{T}}\right] \tag{34}$$

Phase 4: Time Increment

After updating the material point state variables, the grid is reset to the same initial configuration, Figure 2(f). Although the nodal positions are not explicitly updated, resetting the grid results in the movement of the points relative to the nodes.

2.1.5. Timestep

The critical (stable) timestep Δt_{crit} is calculated using the Courant-Friederichs-Lewy (CFL) condition,

$$\Delta t_{\text{crit}} = \frac{h}{\max(c_p + \|\mathbf{v}_p\|)} \tag{35}$$

where h is the grid node spacing, $\mathbf{v}_p$ is the velocity of the material point and c_p is the speed of sound in the material,

$$c_p = \sqrt{\frac{K + \frac{4}{3}G}{\rho}} \tag{36}$$

where $K = \frac{E}{3(1-2\nu)}$ and $G = \frac{E}{2(1+\nu)}$ are the material's bulk and shear modulus respectively, E and ν the Young's modulus and Poisson's ratio and ρ the density.

2.2. Experiments and Models

The setup of the experiments and the MPM models are discussed for the case of a two-dimensional and a three-dimensional sand column, respectively.

2.2.1. Two-Dimensional Sand Column

Lube et al. [22,23] investigated the collapse and runout of a sand column along a horizontal channel as illustrated in Figure 3. The side walls of the channel were constructed from Perspex spaced 200 mm apart in the out-of-plane direction, and a quick-release mechanism was used to remove the gate, Figure 3(a). The initial aspect ratio of the column is defined as $a = {}^{h_i}/_{r_i}$, where h_i is the column height and r_i the column width. The aspect ratio was systematically varied from approximately 0.5 to 20, and the final runout distance r_f measured as shown in Figure 3(b). The normalized runout is defined as $\zeta = {}^{(r_f - r_i)}/_{r_i}$. Based on their experimental results, Lube et al. [22,23] found an empirical relation between the normalized runout and the initial aspect ratio,

$$\zeta(a) = \begin{cases} 1.6a & \text{if } a < 1.8 \\ 2.2a^{2/3} & \text{if } a > 2.8 \end{cases} \tag{37}$$

with is a small transition region for $1.8 < a < 2.8$.

The two-dimensional model, consisting of a base and column, is shown in Figure 3(c)-(d). The base is 20 mm high and the initial width of the column is set to $r_i = 90$ mm. A no-slip condition is

 doi:10.20944/preprints202605.0398.v1

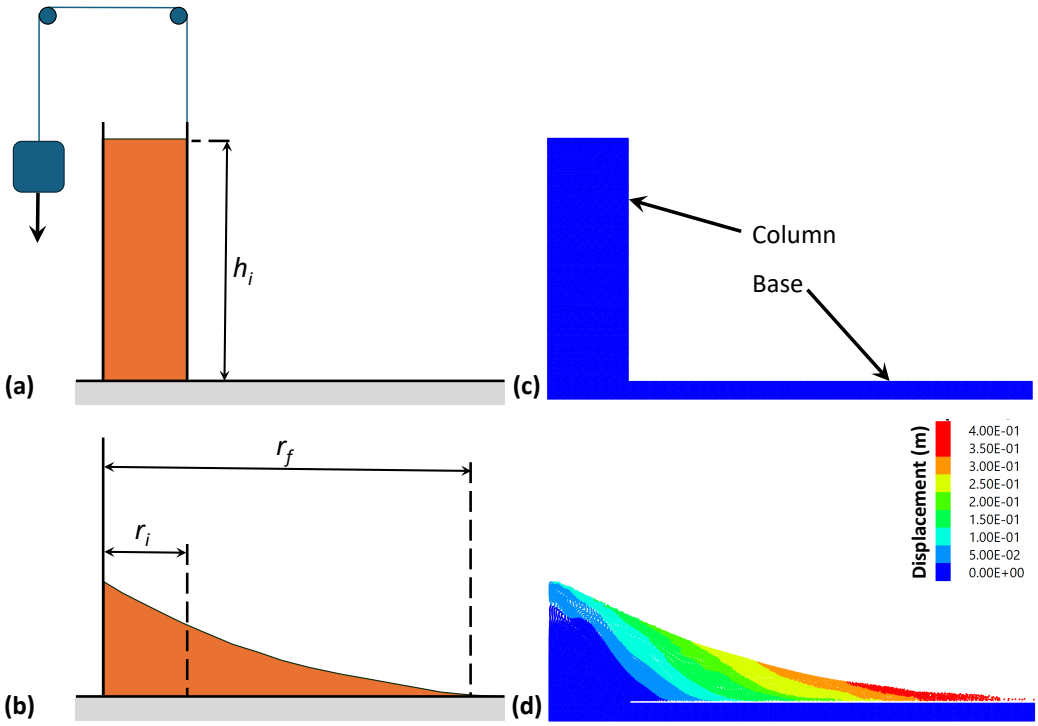

Figure 3. The two-dimensional sand column: (a)-(b) experimental setup adapted from [22] and (c)-(d) a MPM model with $a = 3$ where the colors indicate the displacement magnitude.

applied to the boundary at the bottom of the base and, during the initial phase, a roller condition is applied to the two vertical sides of the column. Initial stresses are first installed under gravity loading using local damping ($\alpha_d = 0.5$). After static equilibrium is reached, the roller boundary condition on the right hand side of the column is removed, simulating the quick removal of the gate in the experiment. During the subsequent flow phase, local damping was set to a low value of $\alpha_d = 0.05$. Due to the nature of MPM, no-slip contact is automatically enforced between the flowing column material and the top of the base. This boundary condition is in agreement with experimental observations of Lube et al. [22,27] who showed that, by using smooth and sandpaper covered basal surfaces, that the surface roughness of the bottom boundary had no significant effect on the runout distance. Their observations showed that a thin layer of grains always forms on the surface, independent of its roughness, and the majority of the material flowed over it.

The sand was modeled as a Mohr-Coulomb material with a density $\rho = 2650\,\mathrm{kg\,m^{-3}}$ [22,25] and the properties calibrated by Fern and Soga [17] as listed in Table 1. The Mohr-Coulomb constitutive model was used, with and without strain softening, and no cohesion. In the strain softening case, two parameter sets were used, one for an initially dense and one for an initially loose sand [17]. The base was modeled as an elastic material with the same density and elastic properties as the sand (E and ν in Table 1).

Table 1. Mohr-Coulomb and strain softening parameters [17].

Parameter	Symbol	Strain Softening		Mohr-Coulomb
		Loose	Dense	
Young's modulus	E	10 MPa	10 MPa	10 MPa
Poisson's ratio	ν	0.2	0.2	0.2
Peak friction angle	ϕ_{peak}	39°	50°	33°
Residual friction angle	ϕ_{res}	33°	33°	-
Maximum dilatancy angle	ψ_{peak}	6°	25°	0°
Residual dilatancy angle	ψ_{res}	0°	0°	-
Shape function	β	4	5	-

 doi:10.20944/preprints202605.0398.v1

2.2.2. Three-Dimensional Sand Column

Similar to the work in Section 2.2.1, Lube et al. [27] performed a series of three-dimensional experiments with a collapsing axis-symmetric column of granular material. Various materials were used, and the column aspect ratios varied from $a = 0.2$ to 35 by changing the column initial radius r_i and height h_i. A Perspex cylinder was used, filled to the desired height, and the column collapse initiated by lifting the cylinder vertically at a speed of $2\,\mathrm{m\,s^{-1}}$, see Figure 4(a-b). The runout distance r_f and final height h_f were measured and various observations regarding the flow patterns were made. An empirical correlation was found relating the normalized runout distance ζ to the initial aspect ratio a [27],

$$\zeta(a) = \begin{cases} 1.24a & \text{if } a < 1.7 \\ 1.6a^{1/2} & \text{if } a > 1.7 \end{cases} \tag{38}$$

The final cone (column) height h_f was found to be,

$$h_f(r_i, a) = \begin{cases} r_i a & \text{if } a < 1 \\ 0.88 r_i a^{1/6} & \text{if } 1.7 < a < 10 \end{cases} \tag{39}$$

Note the transition region $1 < a < 1.7$. The normalized final height $\beta = {}^{h_f}/_{h_i}$ can be written as,

$$\beta(a) = \begin{cases} 1 & \text{if } a < 1 \\ 0.88 a^{-5/6} & \text{if } 1.7 < a < 10 \end{cases} \tag{40}$$

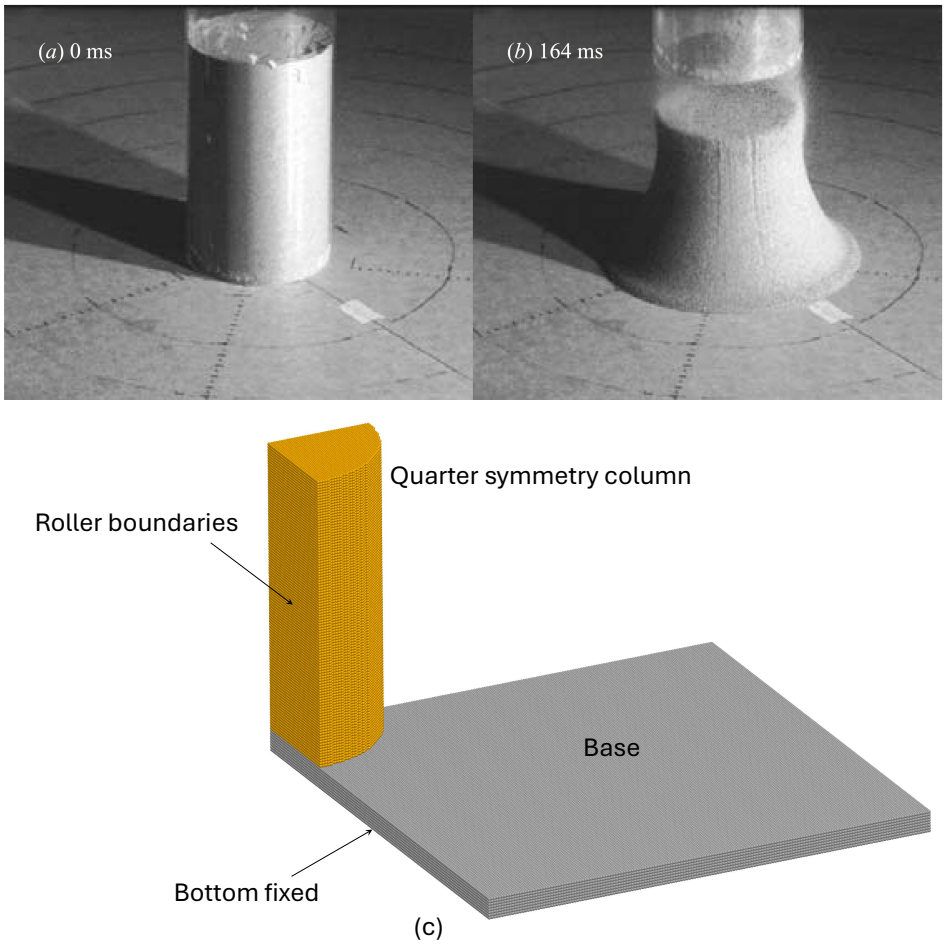

Figure 4. The three-dimensional sand column: (a-b) experimental setup adapted from [27], and (c) the MPM model using quarter symmetry. The experiment and the model shown have an aspect ratio $a = 2.75$.

 doi:10.20944/preprints202605.0398.v1

For comparative purposes, a sand column with an initial radius of $r_i = 97$ mm is modeled, and the initial height h_i is varied to produce aspect ratios ranging from $a = 0.55$ to 7. A quarter-symmetry model is used and roller boundary conditions are applied to the vertical sides. The base was modeled as 20 mm height and fixed at the bottom. The MPM grid spacing is set to 5 mm and initialized with eight material points per cell, see Figure 4(c).

The base and the column have a density of $\rho = 2650\,\mathrm{kg\,m^{-3}}$ [22,25]. The base is modeled as an elastic material with Young's modulus E and Poisson's ratio ν given in Table 1. To initialize the stresses in the column, it is first modeled as an elastic material with the same properties as the base. The local damping is set to $\alpha_d = 0.7$ and the column simulated under gravity to static equilibrium. The column is then assigned a Mohr-Coulomb model (without strain-softening) using the properties given in Table 1, and the local damping set to $\alpha_d = 0.05$ during the collapse and runout phase.

3. Results

The results from the MPM models are compared to the experimental results and observations for the case of a two- and a three-dimensional sand column respectively.

3.1. Two-Dimensional Sand Column

A convergence study is first performed using the Mohr-Coulomb model without strain softening and $a = 1$. The spacing of the MPM background grid nodes is systematically reduced from 10 mm to 1 mm, with four material points per cell initially in all cases. The runout distance and the normalized computation time are shown in Figure 5. Based on these results, a grid spacing of 2 mm is used in all subsequent two-dimensional models.

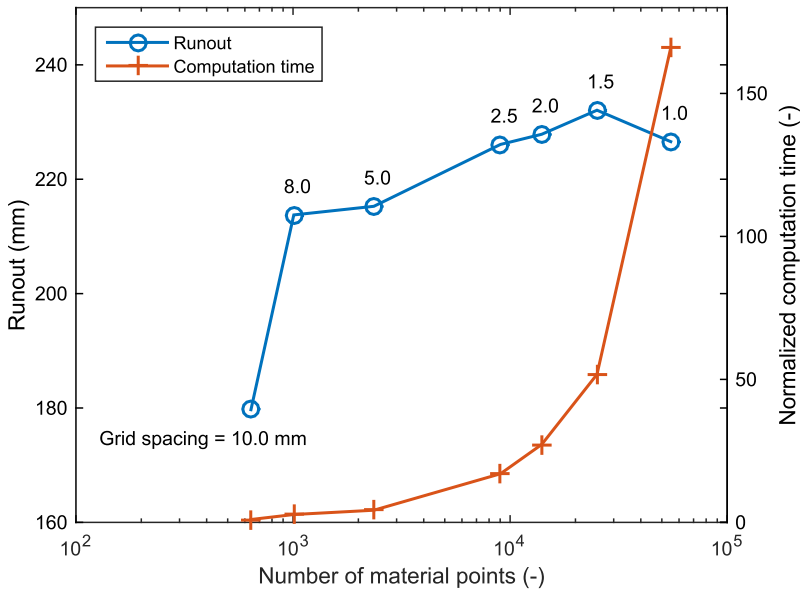

Figure 5. A grid convergence study for the two-dimensional sand column collapse problem. The grid spacing is given for each case and the computation time normalized using the the time from the 10 mm spacing as reference.

The initial column width is kept constant at $r_i = 90$ mm and the height varied to produce aspect ratios ranging from $a = 1$ to 10. The runout results are shown in Figure 6. It is evident that the numerical model accurately predicts the experimental runout distances over the whole range, including the transition region between $a = 1.8$ and 2.8. Compared to the empirical correlation given by Equation 37, the average error in the predicted runout over the whole range is 3.6 %, 5.8 % and 8.9 % for the Mohr-Coulomb and the strain-softening models with properties for a loose and dense sand, respectively. For larger aspect ratios a, the Mohr-Coulomb model without strain-softening produces results most similar to the experimental observations.

 doi:10.20944/preprints202605.0398.v1

The grid spacing is constant at 2 mm with each cell initially populated by four material points. As reference, the number of material points n_p per aspect ratio is also indicated in Figure 6, which ranged from approximately 8000 to 115 000.

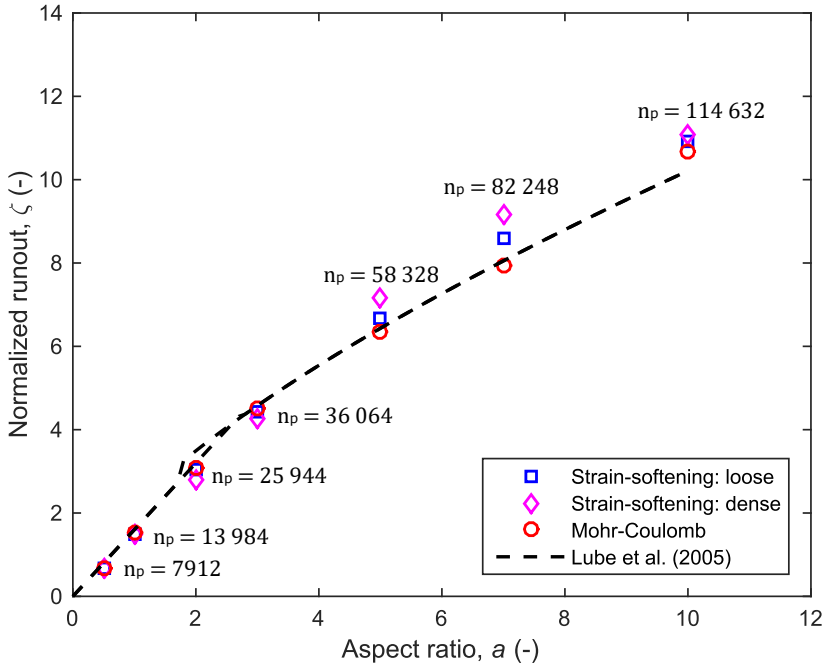

Figure 6. The two-dimensional column collapse and runout showing the effect of the initial aspect ratio a on the normalized runout ζ for various material models and properties. The number of material points is indicated by n_p.

Lube et al. [23] further analyzed the case with an aspect ratio $a = 7$, using a high-speed camera to accurately capture the free-surface profile of the column as it collapsed. Their data has been digitized and plotted at discrete time increments, together with the results from a simulation using the Mohr-Coulomb model without strain-softening. Furthermore, the offset in time between the experiment and the simulation, as determined by [25], has been used to synchronize the results. The results are shown in Figure 7, and the runout distance was accurately modeled during the whole collapse. The height of the column was accurately modeled during the initial stages but was slightly lower than measured during later times. This is similar to the results of [25,26].

3.2. Three-Dimensional Sand Column

The initial column width is kept constant with $r_i = 97$ mm and the height varied to produce aspect ratios ranging from $a = 0.55$ to 7. The runout results are shown in Figure 8, demonstrating that the three-dimensional numerical model accurately predicts the experimentally observed runout over the entire range. Compared to the empirical correlation given by Equation 38, the average error in the predicted runout over the whole range is 3.8 %. The maximum error of 7.8 % is for an aspect ratio of $a = 1.7$, which is at the point where Lube et al. [27] observed a transition in the underlying flow mechanism.

The results of the final height are also shown in Figure 8. For $a < 1$ (Equation 40), the height remains unchanged from the initial height, which the model accurately predicts (normalized height, $\beta \approx 1$). With an increase in the aspect ratio a, the model accurately predicts the decrease in final height. Compared to the empirical correlation given by Equation 39, the average error in the predicted final height over the whole range is only 2.1 %, with a maximum error of 4.1 % for an aspect ratio of $a = 0.9$.

More experimental results are shown in Figure 9(a)-(b) for $a = 0.55$. In that case the empirical prediction for the normalized runout is $\zeta = 1.24 \cdot a = 0.68$ [27]. This is equivalent to a runout distance of 163 mm. Similarly for $a = 0.90$, as shown in Figure 9(e)-(f), the empirical runout distance is 205 mm. The numerical models predict the runout as shown in Figure 9(c) and (g) respectively (not shown to

 doi:10.20944/preprints202605.0398.v1

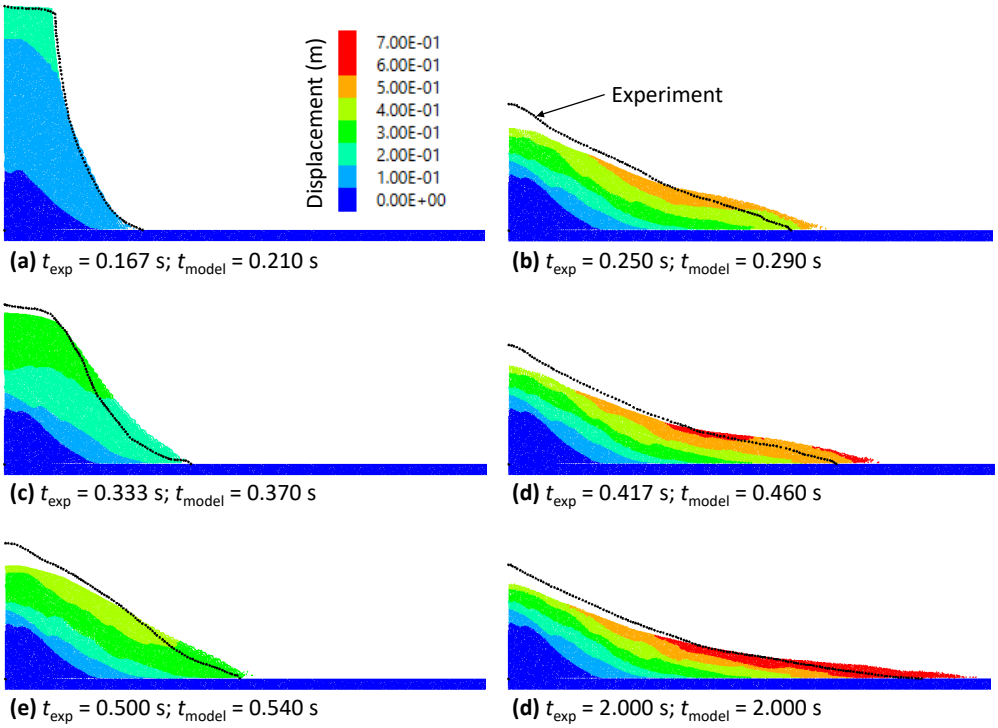

Figure 7. The two-dimensional column showing the collapse at six discrete time intervals, with t_{exp} the time from the experiment [23] and t_{model} the corresponding time in the simulation [25]. The experimentally observed profile of the column is indicated in black and the material points colored according to their displacement magnitude.

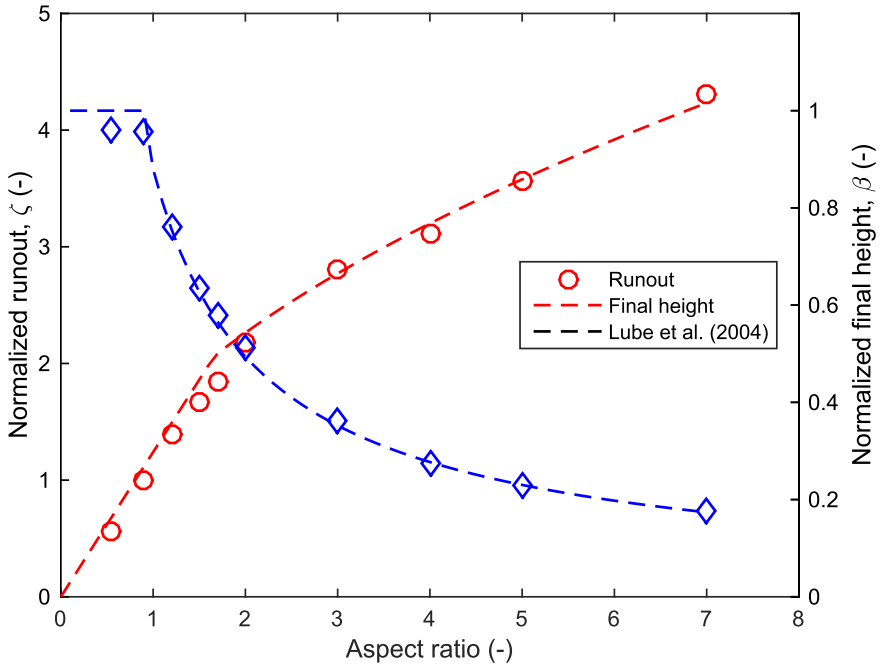

Figure 8. The three-dimensional column collapse and runout showing the effect of the initial aspect ratio a on the normalized runout ζ and the normalized final height β.

 doi:10.20944/preprints202605.0398.v1

the same scale). Figure 9(d) and (h) show the two corresponding top views with the empirical runout indicated by the white radii. The color threshold is set to 1 mm, with all material points that displaced by more than this value colored in red, and all other material points colored in blue.

Lube et al. [27] showed that for a less than approximately one, a circular area of undisturbed material remained preserved at the upper surface of the column, see Figure 9(b). When $a > 1$, the flow eroded the entire column surface which left only a conical pile, see Figure 9(f). The numerical model accurately predicts this behavior with the inner radius of material points remaining largely undisturbed for $a = 0.55$ as shown in Figure 9(c) and (d). For $a = 0.90$, the upper surface of the column is totally eroded as shown in Figure 9(g) and (h).

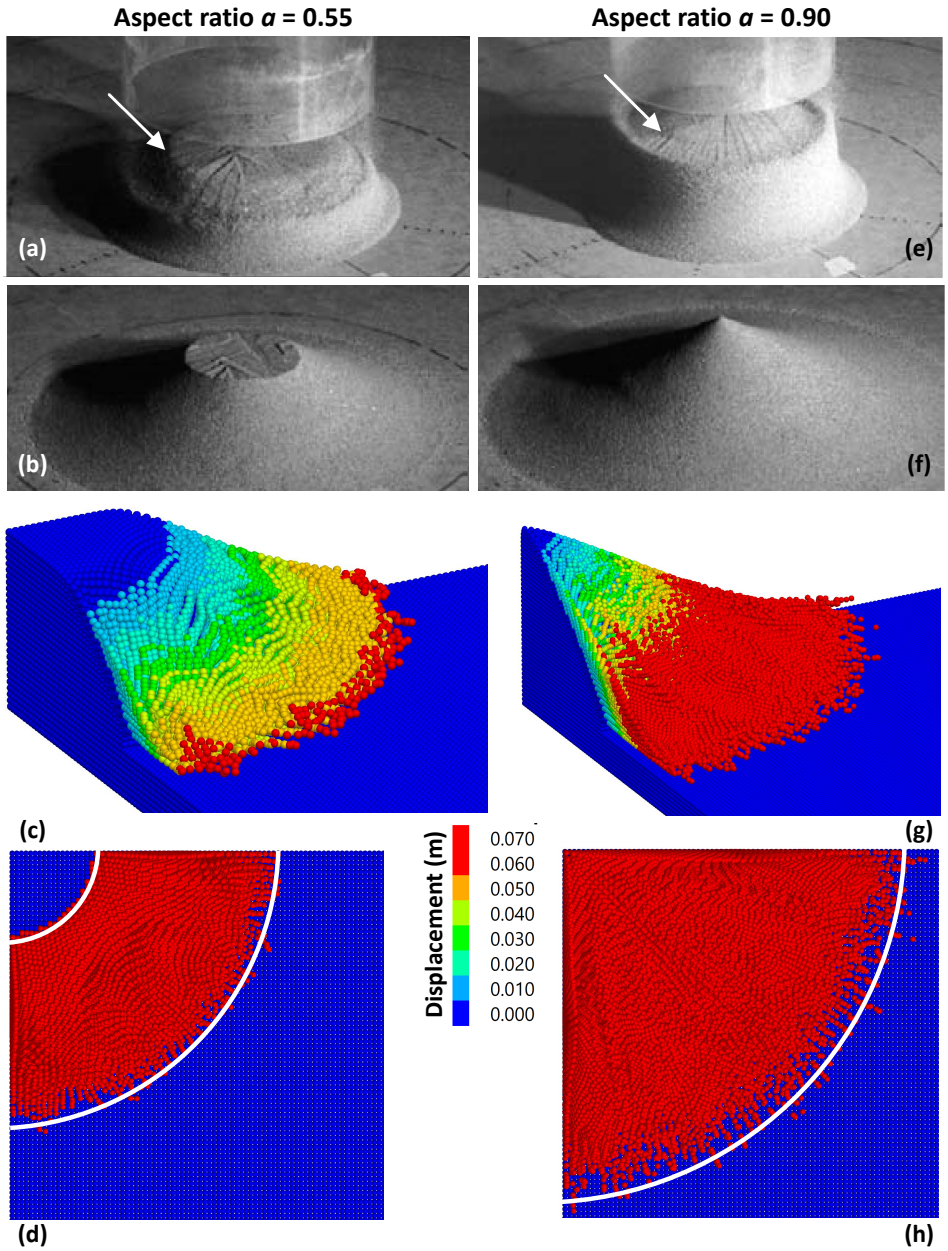

Figure 9. The three-dimensional sand column collapse showing an aspect ratio $a = 0.55$ on the left, and an aspect ratio $a = 0.90$ on the right. The experiment is shown at an intermediate time step (a and e), and the final configuration (b and f) (adapted from [27]). The modeled final configuration is shown in (c) and (g) respectively with the color contours based on the displacement magnitude. The top view of the modeled results are shown in (d) and (h) respectively, with the experimental runout and the remaining radius at the top of the column shown by the white radii, and material points with a displacement of more than 1 mm in red, and all other points in blue.

 doi:10.20944/preprints202605.0398.v1

The grid spacing is kept constant at 5 mm, and each cell initially is populated with eight material points. As reference, the number of material points in the column (ignoring the points in the base layer) ranged from approximately 25 000 to 322 000 for aspect ratios of $a = 0.55$ to 7, respectively.

4. Conclusions

Occurrences such as landslides, slope failures, and avalanches happen suddenly and often without warning. To predict these events and the extent of damage, engineers make use of numerical simulations. During such catastrophic events, the material experiences large deformation and flow, and mesh-based methods such as the finite element method are not capable of modeling it.

This paper shows that the material point method, a particle-based continuum method, can model the collapse and runout of a granular column, which is representative of an event such as a landslide. The model results are compared to laboratory experiments and observations over a wide range of column aspect ratios (initial height to width/radius). It is shown that the model accurately predicts the experimentally observed runout of two- and three-dimensional columns, with error less than 5 %.

The experiments used non-cohesive sand, which has been modeled using the Mohr-Coulomb model with zero cohesion. In the future, the accuracy of this model to predict the collapse and flow of cohesive materials may also be investigated.

Author Contributions: Conceptualization, C.C. and M.P.; methodology, C.C. and M.P.; software development, C.C. and M.P.; validation, C.C. and M.P.; formal analysis, C.C. and M.P.; writing—original draft preparation, C.C.; writing—review and editing, M.P. All authors have read and agreed to the published version of the manuscript.

Funding: This research received no external funding.

Data Availability Statement: Data is available on request.

Acknowledgments: Itasca Consulting Group, Inc. for making the software available.

Conflicts of Interest: The authors declare no conflicts of interest.

References

1. Sulsky, D.; Schreyer, H. A particle method with large rotations applied to the penetration of history-dependent materials. *Advances in Numerical Simulation Techniques for Penetration and Perforation of Solids, ASME* **1993**, *171*.
2. Sulsky, D.; Schreyer, H.L. A particle-in-cell method as a natural impact algorithm. *Advanced Computational Methods for Material Modeling, ASME* **1993**, *AMD-Vol. 1*.
3. Sulsky, D.; Chen, Z.; Schreyer, H.L. A particle method for history-dependent materials. *Comput. Methods Appl. Mech. Engrg.* **1994**, *118*, 179–196.
4. Andersen, S.; Andersen, L. Modelling of landslides with the material-point method. *Computational Geosciences* **2010**, *14*, 137–147. https://doi.org/10.1007/s10596-009-9137-y.
5. Wang, B.; Hicks, M.A.; Vardon, P.J. *Slope failure analysis using the random material point method*; Vol. 6, 2016; pp. 1–6. https://doi.org/10.1680/jgele.16.00019.
6. Septian, A.; Llano-Serna, M.A.; Ruest, M.R.; Williams, D.J. Three-dimensional Kinematic Analysis of Bingham Canyon Mine Pit Wall Slides. *Procedia Engineering* **2017**, *175*, 86–93. https://doi.org/10.1016/j.proeng.2017.01.030.
7. Troncone, A.; Conte, E.; Pugliese, L. Analysis of the slope response to an increase in pore water pressure using the material point method. *Water (Switzerland)* **2019**, *11*, 1–14. https://doi.org/10.3390/w11071446.
8. Zhao, L.; Qiao, N.; Zhao, Z.; Zuo, S.; Wang, X. Comparative study of material point method and upper bound limit analysis in slope stability analysis. *Transportation Safety and Environment* **2020**, *2*, 44–57. https://doi.org/10.1093/tse/tdaa002.
9. Nguyen, T.S.; Yang, K.H.; Ho, C.C.; Huang, F.C. Postfailure Characterization of Shallow Landslides Using the Material Point Method. *Geofluids* **2021**, *2021*. https://doi.org/10.1155/2021/8860517.
10. Toro Rojas, D.; Cordão Neto, M.P.; Muniz de Farias, M.; Lorenzo Reynaldo, R. Analysis of the failure modes and development of landslides using the material point method. *Soils and Rocks* **2021**, *44*, 1–13. https://doi.org/10.28927/sr.2021.057820.

 doi:10.20944/preprints202605.0398.v1

11. He, K.; Xi, C.; Liu, B.; Hu, X.; Luo, G.; Ma, G.; Zhou, R. MPM-based mechanism and runout analysis of a compound reactivated landslide. *Computers and Geotechnics* **2023**, *159*, 105455. https://doi.org/10.1016/j.compgeo.2023.105455.
12. Zhang, W.; Wu, Z.; Peng, C.; Li, S.; Dong, Y.; Yuan, W. Modelling large-scale landslide using a GPU-accelerated 3D MPM with an efficient terrain contact algorithm. *Computers and Geotechnics* **2023**, *158*, 105411. https://doi.org/10.1016/j.compgeo.2023.105411.
13. Fernández, F.; Vargas, E.; Muller, A.L.; Sousa, R.L.; e Sousa, L.R.; Fernández, F.; Vargas, E.; Muller, A.L.; Sousa, R.L.; e Sousa, L.R. Material point method modeling in 3D of the failure and run-out processes of the Daguangbao landslide. *Acta Geotechnica* **2024**, *19*, 4277–4296. https://doi.org/10.1007/s11440-023-02152-4.
14. Mast, C.M. Modeling Landslide-Induced Flow Interactions with Structures using the Material Point Method. Phd, University of Washington, 2013.
15. Zhang, X.; Krabbenhoft, K.; Pedroso, D.M.; Lyamin, A.V.; Sheng, D.; da Silva, M.V.; Wang, D. Particle finite element analysis of large deformation and granular flow problems. *Computers and Geotechnics* **2013**, *54*, 133–142. https://doi.org/10.1016/j.compgeo.2013.07.001.
16. Bandara, S. Material Point Method to simulate Large Deformation Problems in Fluid-saturated Granular Medium. Phd, University of Cambridge, 2013.
17. Fern, E.J.; Soga, K. The role of constitutive models in MPM simulations of granular column collapses. *Acta Geotechnica* **2016**, *11*, 659–678. https://doi.org/10.1007/s11440-016-0436-x.
18. Fern, E.J.; Soga, K. Granular Column Collapse of Wet Sand. *Procedia Engineering* **2017**, *175*, 14–20. https://doi.org/10.1016/j.proeng.2017.01.005.
19. Ceccato, F.; Leonardi, A.; Girardi, V.; Simonini, P.; Pirulli, M. Numerical and experimental investigation of saturated granular column collapse in air. *Soils and Foundations* **2020**, *60*, 683–696. https://doi.org/10.1016/j.sandf.2020.04.004.
20. Sordo, B.; Rathje, E.; Kumar, K. Sequential Hybrid Finite Element and Material Point Method to Simulate Slope Failures. *Computers and Geotechnics* **2024**, *173*, 106525. https://doi.org/10.1016/j.compgeo.2024.106525.
21. Zhan, Z.Q.; Zhou, C.; Cai, G.L.; Liu, C.Q.; Liu, J.Q.; Wu, Y. Physical and MPM modelling of sand column collapse with different moisture and density conditions. *Powder Technology* **2026**, *467*. https://doi.org/10.1016/j.powtec.2025.121572.
22. Lube, G.; Huppert, H.E.; Sparks, R.S.J.; Freundt, A. Collapses of two-dimensional granular columns. *Physical Review E - Statistical, Nonlinear, and Soft Matter Physics* **2005**, *72*. https://doi.org/10.1103/PhysRevE.72.041301.
23. Lube, G.; Huppert, H.E.; Sparks, R.S.; Freundt, A. Static and flowing regions in granular collapses down channels. *Physics of Fluids* **2007**, *19*, 1–10. https://doi.org/10.1063/1.2712431.
24. Sołowski, W.T.; Sloan, S.W. Modelling of sand column collapse with material point method. *Computational Geomechanics, COMGEO III - Proceedings of the 3nd International Symposium on Computational Geomechanics* **2013**, *553*, 698–705.
25. Solowski, W.; Sloan, S. Evaluation of material point method for use in geotechnics. *International Journal for Numerical and Analytical Methods in Geomechanics* **2015**, *39*, 685–701.
26. Hamad, F.; Stolle, D.; Moormann, C. Material point modelling of releasing geocontainers from a barge. *Geotextiles and Geomembranes* **2016**, *44*, 308–318. https://doi.org/10.1016/j.geotexmem.2015.12.005.
27. Lube, G.; Huppert, H.E.; Sparks, R.S.J.; Hallworth, M.A. Axisymmetric collapses of granular columns. *Journal of Fluid Mechanics* **2004**, *508*, 175–199. https://doi.org/10.1017/S0022112004009036.
28. Nguyen, V.P. Material point method: basics and applications. Technical report, neering, Institute of Advanced Mechanics and Materials, 2014.
29. Sulsky, D.L.; Zhou, S.L.L.; Schreyer, H.L. Application of a particle-in-cell method to solid mechanics. *Computer Physics Communications* **1995**, *87*, 236–252.
30. Steffen, M.; Kirby, R.M.; Berzins, M. Decoupling and balancing of space and time errors in the material point method (MPM). *International Journal for Numerical Methods in Engineering* **2010**, *82*, 1207–1243. https://doi.org/10.1002/nme.2787.
31. De Vaucorbeil, A.; Nguyen, V.P.; Sinaie, S.; Wu, J.Y. Material point method after 25 years: Theory, implementation, and applications. *Advances in Applied Mechanics* **2020**, *53*, 185–398. https://doi.org/10.1016/bs.aams.2019.11.001.
32. Steffen, M.; Kirby, R.M.; Berzins, M. Analysis and reduction of quadrature errors in the material point method (MPM). *International Journal for Numerical Methods in Engineering* **2008**, *76*, 922–948. https://doi.org/10.1002/nme.2360.

 doi:10.20944/preprints202605.0398.v1

33. Steffen, M.; Wallstedt, P.C.; Guilkey, J.E.; Kirby, R.M.; Berzins, M. Examination and analysis of implementation choices within the Material Point Method (MPM). *CMES - Computer Modeling in Engineering and Sciences* **2008**, *31*, 107–127. https://doi.org/10.3970/cmes.2008.031.107.
34. Steffen, M. Analysis-guided improvements of the material point method. Phd, The University of Utah, 2009.
35. Nakamura, K.; Matsumura, S.; Mizutani, T. Taylor particle-in-cell transfer and kernel correction for material point method. *Computer Methods in Applied Mechanics and Engineering* **2023**, *403*, 115720. https://doi.org/10.1016/j.cma.2022.115720.
36. Wallstedt, P.C.; Guilkey, J.E. Improved velocity projection for the material point method. *CMES - Computer Modeling in Engineering and Sciences* **2007**, *19*, 223–232. https://doi.org/10.3970/cmes.2007.019.223.
37. Duverger, S.; Duriez, J.; Philippe, P.; Bonelli, S. Critical Comparison of Motion Integration Strategies and Discretization Choices in the Material Point Method. *Archives of Computational Methods in Engineering* **2025**, *32*, 1369–1397. https://doi.org/10.1007/s11831-024-10170-y.
38. FLAC. Fast Lagrangian Analysis of Continua, Version 9.6, Itasca Consulting Group, Inc., Minneapolis, USA, 2026.
39. Nairn, J.A. Numerical simulation of orthogonal cutting using the material point method. *Engineering Fracture Mechanics* **2015**, *149*, 262–275. https://doi.org/10.1016/j.engfracmech.2015.07.014.